Recognition of Ribonuclease A by 3′–5′-Pyrophosphate-Linked Dinucleotide Inhibitors: A Molecular Dynamics/Continuum Electrostatics Analysis

Savvas Polydoridis,* Demetres D. Leonidas,† Nikos G. Oikonomakos,†‡ and Georgios Archontis*‡
*Department of Physics, University of Cyprus, Nicosia, Cyprus; and †Institute of Organic and Pharmaceutical Chemistry, ‡Institute of Biological Research and Biotechnology, the National Hellenic Research Foundation, Athens, Greece

ABSTRACT The proteins of the pancreatic ribonuclease A (RNase A) family catalyze the cleavage of the RNA polymer chain. The development of RNase inhibitors is of significant interest, as some of these compounds may have a therapeutic effect in pathological conditions associated with these proteins. The most potent low molecular weight inhibitor of RNase reported to date is the compound 5′-phospho-2′-deoxyuridine-3-pyrophosphate (P→5)-adenosine-3-phosphate (pdUppA-3′-p). The 3′,5′-pyrophosphate group of this compound increases its affinity and introduces structural features which seem to be unique in pyrophosphate-containing ligands bound to RNase A, such as the adoption of a syn conformation by the adenosine base at RNase subsite B_2 and the placement of the 5′-β-phosphate of the adenylate (instead of the α-phosphate) at subsite P_1 where the phosphodiester bond cleavage occurs. In this work, we study by multi-ns molecular dynamics simulations the structural properties of RNase A complexes with the ligand pdUppA-3′-p and the related weaker inhibitor dUppA, which lacks the 3′ and 5′ terminal phosphate groups of pdUppA-3′-p. The simulations show that the adenylate 5′-β-phosphate binding position and the adenosine syn orientation constitute robust structural features in both complexes, stabilized by persistent interactions with specific active-site residues of subsites P_1 and B_2. The simulation structures are used in conjunction with a continuum-electrostatics (Poisson-Boltzmann) model, to evaluate the relative binding affinity of the two complexes. The computed relative affinity of pdUppA-3′-p varies between −7.9 kcal/mol and −2.8 kcal/mol for a range of protein/ligand dielectric constants (ϵ_p) 2–20, in good agreement with the experimental value (−3.6 kcal/mol); the agreement becomes exact with $\epsilon_p = 8$. The success of the continuum-electrostatics model suggests that the differences in affinity of the two ligands originate mainly from electrostatic interactions. A residue decomposition of the electrostatic free energies shows that the terminal phosphate groups of pdUppA-3′-p make increased interactions with residues Lys^7 and Lys^{66} of the more remote sites P_2 and P_0, and His^{119} of site P_1.

INTRODUCTION

The pancreatic ribonuclease A (RNase A) family contains proteins, which decompose the RNA polymer chain (1,2). Many members of the family display pathological side effects. For example, human angiogenin (3) is implicated in cancer and in vascular and rheumatoid diseases (4); eosinophil-derived neurotoxin and eosinophil cationic protein are neurotoxic in vivo and are involved in hypereosinophilic syndromes and allergy (5); and bovine seminal RNase has antispermatogenic and immunosuppressive activity (6). The activity of these proteins is critically affected by mutations of residues involved in ribonucleolysis, or by ribonucleolytic inhibitors (3,7,8). Thus, the development of RNase inhibitors is of significant interest, as some of these compounds may act as therapeutic agents in pathological conditions associated with these proteins.

The RNase A catalytic site with a bound RNA molecule is shown schematically in Fig. 1. According to the established nomenclature (2), the active site is partitioned into subsites $\{B_i\}$ and $\{P_i\}$, which interact, respectively, with the RNA bases and phosphate groups. Subsite B_1 has a strong specificity for pyrimidine bases, conferred by residue Thr^{45}, which is strictly conserved in all RNases. The protein cleaves the P-O5′ (scissile) bond on the 3′ side of pyrimidine bases bound at B_1. Residues His^{12}, His^{119}, and Lys^{41} (subsite P_1) are strictly conserved among RNase homologs and play key roles in the reaction (2,9). Subsite B_2 recognizes all bases, with a preference for adenine. It is highly conserved, but other subsites are more variable among homologs.

The high degree of B_1, P_1, and B_2 homology suggests that inhibitors of one protein may also act against other members of the same family. Based on this expectation, structure-assisted inhibitor design studies have mainly focused on RNase A. Structural and kinetic studies have examined the complexes between RNase A and several mono- or dinucleotide inhibitors containing adenine (10–17) or inosine (18) at the 3′ position of the scissile bond, and uracil (13–17) or cytosine (11,12) at the 5′ position. The high-resolution structures of several complexes have provided a detailed picture of the inhibitor binding modes.

The most potent inhibitors (13–17) contain a nonstandard pyrophosphate group, which increases the affinity of nucleotide ligands by two orders of magnitude (14). Compounds

Submitted July 18, 2006, and accepted for publication November 1, 2006.

Address reprint requests to G. Archontis, E-mail: archonti@ucy.ac.cy.

Abbreviations used: dUppA, 2′-deoxyuridine-3-pyrophosphate (P→5) adenosine; pdUppA-3′-p, 5′-phospho-2′-deoxyuridine-3-pyrophosphate (P→5)-adenosine-3-phosphate; and ppA-2′-p, 5′-diphosphoadenosine 2′-phosphate; and ppA-3′-p, 5′-diphosphoadenosine 3′-phosphate.

© 2007 by the Biophysical Society

0006-3495/07/03/1659/14 $2.00 doi: 10.1529/biophysj.106.093419

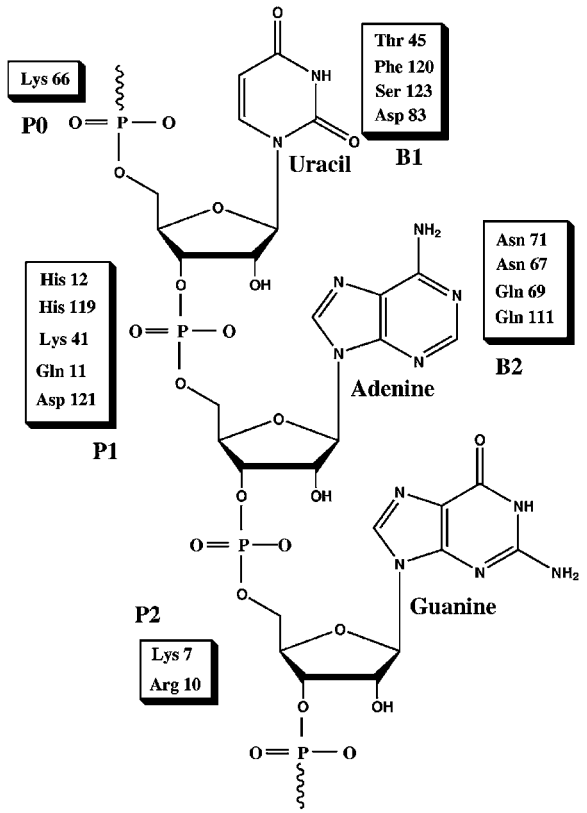

FIGURE 1 Schematic representation of the RNase A active site, with a bound RNA ligand. The subsites $\{B_i\}$ and $\{P_i\}$, interacting, respectively, with the RNA bases and phosphate groups are indicated. The figure is adapted from Raines (2).

ppA-3′-p ($K_i = 240$ nM) and ppA-2′-p ($K_i = 520$ nM) were the first inhibitors with this group (13,14). The compounds bind to RNase A with the β-phosphate at site P_1 and the adenosine χ angle in the syn range (13), structural features that are unique to pyrophosphate-containing ligands (15–17). Both inhibitors are strong, but do not make use of residues at subsites B_1 and P_0. To exploit potential interactions with these sites, a 2′-deoxy-5′-phosphoyuridine group was added to ppA-3′-p to create the new ligand pdUppA-3′-p. The uridine moiety of pdUppA-3′-p made numerous van der Waals and hydrogen-bonding interactions with the RNase A B_1 and the 5′-phosphate made medium-range Coulombic interactions with the Lys^{66} NZ group at the P_0 site; a hydrogen bond between the two groups could not be ruled out from the crystal structure (15). Compound pdUppA-3′-p is a ninefold stronger inhibitor than ppA-3′-p and the most potent RNase inhibitor to date, with a K_i of 27 nm. It is also effective against eosinophil-derived neurotoxin and RNase-4, with respective K_i values of 180 nM and 260 nM.

In this work we investigate for the first time by multi-nanosecond simulations in explicit water the dynamical behavior of RNase A complexes with two pyrophosphate compounds: 1), the most potent inhibitor pdUppA-3′-p; and 2), the related compound dUppA (16), which lacks the 3′, 5′ phosphate groups of pdUppA-3′-p and has a K_i of 11.3 μM for RNase A (16), corresponding to a weaker affinity by 3.6 kcal/mol. The chemical structures of the two molecules are shown in Fig. 2. The simulations reproduce essential features of the crystallographic structures, and provide insights on the flexibility of the bound ligands and the surrounding active-site residues.

The accurate computation of relative (19–26) or absolute (27–33) binding affinities has important applications in protein-ligand docking and design, and has attracted considerable computational effort in recent years. In this work, we evaluate the relative binding affinity of the two RNase A complexes by using the simulation conformations in conjunction with a continuum-electrostatics (Poisson-Boltzmann) approximation (34–37). This continuum model yields results in very good agreement with experiment, suggesting that the electrostatic interactions contribute mostly to the stability differences between the two complexes. We also evaluate the contribution to binding due to specific protein-ligand interactions and desolvation terms by a free-energy decomposition analysis of the Poisson-Boltzmann free energies (38,39).

In the next section, we describe the simulation methods and the continuum model. The results are given in the following section. The final section discusses the results and summarizes the conclusions.

THEORY AND METHODS

Molecular dynamics simulations

The crystallographic structures of the pdUppA-3′-p and dUppA complex have been determined at a resolution of 1.7 Å. The initial protein coordinates were taken from these structures (accession codes 1QHC (15) and 1JN4 (16)). The simulation system corresponded to a 29 Å sphere containing the entire protein, the ligand, and 2997 water molecules. The sphere was centered on the PB atom of the ligand. The water environment was created by retaining 135 crystallographic waters; additional water molecules were included by overlaying a preequilibrated 32 Å water sphere on the complex and deleting waters beyond 29 Å from the center of the complex, or overlapping with protein-heavy atoms or crystallographic-water oxygen atoms. This overlaying procedure was repeated 2–3 times during the equilibration of the two complexes.

Atomic charges, van der Waals, and force-field parameters corresponded to the CHARMM22 all-atom force field (40). The water was reproduced by a modified TIP3P water model (41). Electrostatic interactions were calculated by use of a multipole approximation (extended electrostatics) for groups >14 Å apart (42); van der Waals interactions were switched to zero at distances >12 Å. Water molecules were restrained to a spherical region of 29 Å radius by the stochastic boundary method (43). Water oxygen atoms in a buffer beyond 23 Å from the center were subjected to random and frictional forces mimicking a thermal bath at 293 Kelvin (44). Protein heavy atoms beyond 16 Å from the center were harmonically restrained, based on the crystallographic B-factors. Bond lengths with hydrogen atoms, and the geometry of water molecules were constrained by the SHAKE algorithm (45). The classical equations of motion were integrated by a Verlet algorithm modified for Langevin dynamics, using a time step of 1 fs.

To minimize structural perturbations in the molecular dynamics (MD) simulations due to the omission of the bulk solvent beyond the simulation

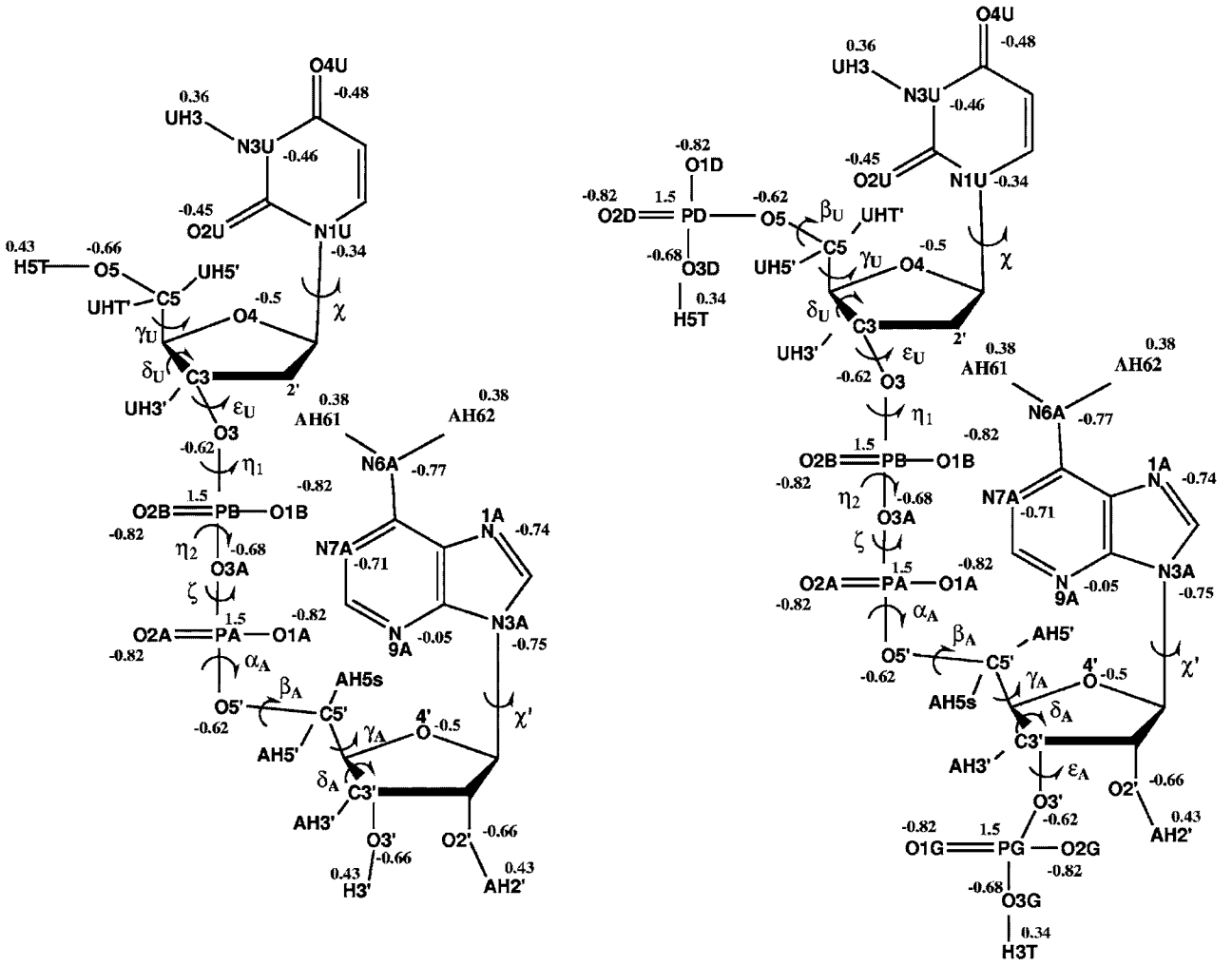

FIGURE 2 Chemical structures of the compounds dUppA (*a*) and pdUppA-3′-p (*b*). The atomic names and charges and the torsional angles discussed in the text are indicated.

sphere, the atomic charges of selected residues were scaled by a robust inhomogeneous reaction-field methodology, presented in Simonson et al. (46) and tested in detail in the aspartyl-tRNA synthetase system in the literature (46–48). All residues treated by this scheme did not participate in salt bridges and were located at least 20 Å away from the central phyrophosphate group of either ligand, and at least 14.5 Å from the nearest terminal (5′) phosphate group of pdUppA-3′-p. The scaled residues (scaling factors) were Lys^{31}(4.31), Lys^{61}(4.15), Arg^{85}(2.08), Lys^{91}(4.63), Lys^{98}(2.85), and His^{105}(2.39). The charges of side-chain atoms in these residues were divided by the corresponding scaling factor. The resulting simulation system had a total charge ≈0 for the dUppA complex.

In the crystallographic structures of the two complexes (15,16) there is no electronic density associated with bound ions. Thus, the structural features of the two complexes are not expected to depend on specific interactions with solution ions, located at well-defined positions. In the MD simulations, the solution screening of electrostatic interactions was taken into account by the scaling factors described above, without explicit counterions. In the Poisson-Boltzmann (PB) calculations (below), the average ionic effect is taken into account by setting the ionic concentration to the experimental ionic strength of 0.2 M.

The simulations had a first, 400-ps equilibration phase. In the subsequent 4-ns production phase, the protein and solvent coordinates were saved every 1 ps for analysis. All simulations were performed with the CHARMM biomolecular program (49), Ver. c28b1.

Poisson-Boltzmann calculations

To calculate the continuum-electrostatics free energies of binding for the various protein-ligand complexes, we evaluated the electrostatic potentials for the protein alone, the ligand alone, and the protein-ligand complex by solving the finite-difference Poisson equation on a three-dimensional grid. For the three states (protein, ligand, complex) the same three-dimensional grid and the same coordinates were used, so that the molecules were localized in the same positions on the grid. This allowed artificial contributions to the potential arising from the grid to be subtracted out exactly (50).

Finite-difference Poisson calculations were done for multiple (usually 200) structures taken from the 4 ns molecular dynamics trajectories of the two complexes. Averaging over multiple structures was expected to improve the precision and accuracy of the FDPB results (19,51). For each structure, the Poisson-Boltzmann equation was solved first on a large, coarse grid (0.8 Å spacing, 72–80 Å side), with screened Coulombic potentials on the grid boundary, and then on a finer grid (0.4 Å spacing, 56–64 Å side) with the coarse solution as boundary conditions (focusing method (50)). The sizes of

the coarser grid were chosen so that a high-dielectric layer of minimal width 20 Å would surround the complex. The dielectric constant of the solvent was set to 80. These of the protein and ligand were taken to be equal; values of 1–20 were compared. Atomic radii and charges were taken from the CHARMM22 force field used in the MD simulations, with the exception of the hydrogen radii, which were set to 1.0 Å. The protein-solvent boundary was defined by the molecular surface, constructed using a solvent probe radius of 2 Å. The ionic strength was set to the experimental value 0.2 M of monovalent counterions. Additional calculations were performed at 0 M, to check the dependence of the results on ionic concentration. All calculations were performed with the UHBD program (52).

Electrostatic free energy component analysis

The derivation of the electrostatic components has been presented in Archontis et al. (39) (see also (38)). We include it here, for the sake of convenience of the reader.

The electrostatic free energy of a protein-ligand complex (PL) is given by the expression (39,53)

$$G^{\mathrm{PL}} = \frac{1}{2}\sum_{\mathrm{i}\in\mathrm{prot,lig}} q_{\mathrm{i}}V_{\mathrm{i}}^{\mathrm{PL}} = \frac{1}{2}\sum_{\mathrm{i}\in\mathrm{prot}} q_{\mathrm{i}}V_{\mathrm{i}}^{\mathrm{PL}} + \frac{1}{2}\sum_{\mathrm{i}\in\mathrm{lig}} q_{\mathrm{i}}V_{\mathrm{i}}^{\mathrm{PL}}, \qquad (1)$$

where q_{i} is the charge on atom i of the protein or ligand, and $V_{\mathrm{i}}^{\mathrm{PL}}$ is the electrostatic potential on atom i, in the solvated complex PL; analogous expressions yield the electrostatic free energies of the isolated protein (P) and ligand (L).

The total electrostatic potential on atom i inside the complex PL can be expressed as a sum over contributions from all ligand and protein atoms

$$V_{\mathrm{i}}^{\mathrm{PL}} = \sum_{\mathrm{j}\in\mathrm{lig}} V_{\mathrm{j}\to\mathrm{i}}^{\mathrm{PL}} + \sum_{\mathrm{j}\in\mathrm{prot}} V_{\mathrm{j}\to\mathrm{i}}^{\mathrm{PL}}, \qquad (2)$$

with $V_{\mathrm{j}\to\mathrm{i}}^{\mathrm{PL}}$ the potential on atom i due to atom j in the complex PL. Using this decomposition and the reciprocity relation $q_{\mathrm{i}}V_{\mathrm{j}\to\mathrm{i}}^{\mathrm{PL}} = q_{\mathrm{j}}V_{\mathrm{i}\to\mathrm{j}}^{\mathrm{PL}}$ (53), we arrive at the following expression for the electrostatic free energy of the complex:

$$G^{\mathrm{PL}} = \frac{1}{2}\sum_{\mathrm{i}\in\mathrm{prot,j}\in\mathrm{prot}} q_{\mathrm{i}}V_{\mathrm{j}\to\mathrm{i}}^{\mathrm{PL}} + \frac{1}{2}\sum_{\mathrm{i}\in\mathrm{lig,j}\in\mathrm{lig}} q_{\mathrm{i}}V_{\mathrm{j}\to\mathrm{i}}^{\mathrm{PL}} + \sum_{\mathrm{i}\in\mathrm{prot,j}\in\mathrm{lig}} q_{\mathrm{i}}V_{\mathrm{j}\to\mathrm{i}}^{\mathrm{PL}}. \qquad (3)$$

The electrostatic binding free energy of the complex PL, ΔG_{bind}, is equal to the difference between the free energies of the complex and the isolated protein and ligand in solution,

$$\Delta G_{\mathrm{bind}} = G^{\mathrm{PL}} - G^{\mathrm{P}} - G^{\mathrm{L}}. \qquad (4)$$

With the aid of Eq. 3, we obtain for ΔG_{bind} (38,39):

$$\begin{aligned}\Delta G_{\mathrm{bind}} &= \sum_{\mathrm{i}\in\mathrm{prot,j}\in\mathrm{lig}} q_{\mathrm{i}}V_{\mathrm{j}\to\mathrm{i}}^{\mathrm{PL}} + \frac{1}{2}\sum_{\mathrm{i}\in\mathrm{lig,j}\in\mathrm{lig}} q_{\mathrm{i}}[V_{\mathrm{j}\to\mathrm{i}}^{\mathrm{PL}} - V_{\mathrm{j}\to\mathrm{i}}^{\mathrm{L}}] \\ &\quad + \frac{1}{2}\sum_{\mathrm{i}\in\mathrm{prot,j}\in\mathrm{prot}} q_{\mathrm{i}}[V_{\mathrm{j}\to\mathrm{i}}^{\mathrm{PL}} - V_{\mathrm{j}\to\mathrm{i}}^{\mathrm{P}}] \\ &\equiv \Delta G_{\mathrm{int}}^{\mathrm{PL}} + \Delta G_{\mathrm{desolv}}^{\mathrm{L}} + \Delta G_{\mathrm{desolv}}^{\mathrm{P}}. \qquad (5)\end{aligned}$$

The first term on the right-hand side of the Eq. 5 is a free-energy component associated with the direct interaction between protein and ligand charges in the solvated complex. The second term corresponds to the ligand desolvation component, i.e., the change in the intraligand interactions upon binding, due to changes in the ligand geometry or charge distribution, as well as changes in the interaction of the ligand with polarization charge in the surrounding medium. If the ligand is assumed to have the same geometry and partial charges in the free and bound state (as here), this term arises entirely from ligand interactions with the polarization charge. The last term has an identical interpretation for the protein (38,39).

RESULTS

We first discuss the dynamical behavior of the two complexes and describe the important ligand-protein interactions observed in the simulations. We then evaluate the relative electrostatic binding free energy of the two complexes by a Poisson-Boltzmann approximation, and identify the protein residues, which mostly contribute to the stabilization of pdUppA-3′-p with respect to dUppA by a free-energy component analysis (38,39).

Simulation structures and interactions

Complex with dUppa

The Cartesian-coordinate root-mean-square (RMS) deviation from the initial conformation is plotted in Fig. 3 as a function of the simulation time. Note that $t = 0$ corresponds to the beginning of the production period, i.e., after 400 ps of equilibration. The left and right panels show, respectively, the dUppA and pdUppA-3′-p complex results. The total RMS deviation of the protein backbone heavy atoms (Fig. 3 *A*) is ≈0.65 Å at the end of the 4-ns production period (4.4 ns total time), showing that the protein conformation remains in the close vicinity of the crystal structure.

The ligand conformations can be described by a set of dihedral angles, defined in Fig. 2. The glycosyl dihedral angles χ and χ' describe, respectively, the orientation of the uracil and adenine rings, and the angles ϵ_{U}, η_1, η_2, ζ, and α_{A} characterize the conformation of the ligand pyrophosphate group. The time evolution of these dihedral angles is shown in Fig. 4 and the average values are listed in Table 1; for dihedrals, which fluctuate in more than one basin, we compute separately and report the average value in each basin.

The time series of the glycosyl dihedral angles χ and χ' for the dUppA ligand correspond to the solid curves in Fig. 4 *A*. The fluctuations in the χ' angle are very small, signifying that the χ' syn conformation is very stable throughout the simulation; this conformation is observed in all RNase complexes with the pyrophosphate-containing ligands dUppA (16), pdUppA-3′-p (15), and ppA-3′-p (13). The χ fluctuations are somewhat larger; however, the conformations of both adenine and uracil rings stay close to the initial (x ray) structure, with an RMS deviation of 0.7–0.8 Å at the end of the 4-ns production period (Fig. 3 *B*) and an average RMS positional fluctuation of ≈0.6 Å.

The pyrophosphate backbone is somewhat more flexible; the phosphate dihedrals η_1, η_2, ζ, and α_{A} fluctuate in the vicinity of the x-ray values and around different rotamers (Fig. 4 *B* and Table 1). The overall RMS positional fluctuation of the pyrophosphate atoms ranges between 0.45 Å and 0.85 Å. Atom PB has the smallest RMS fluctuation (0.45 Å), and a 0.6 Å RMS deviation from its initial position (Fig. 3 *C*). Thus, the PB position is very stable, in accord with the observation that all pyrophosphate-containing ligands bind with this phosphate at the P_1 site (13,15–17). The RMS

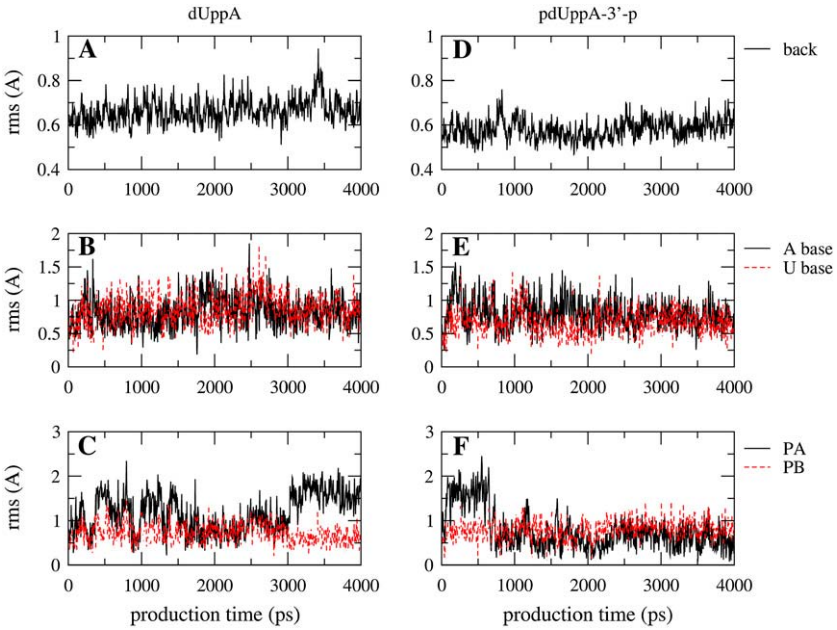

FIGURE 3 Root-mean-square deviation of selected groups of atoms from the starting conformation, plotted as a function of the simulation time. The $t = 0$ value corresponds to the end of the equilibration phase (400 ps). The results for complex dUppA are shown in plots *A–C*; those for pdUppA-3′-p are in plots *D–F*. Plots *A* and *D* are protein main chain heavy atoms; plots *B* and *E* are adenine and uracil ring atoms. Plots *C* and *F* are phosphate PA and PB atoms. The net rotation and translation has been removed, by orienting all trajectory frames with respect to the initial atomic coordinates of the protein backbone heavy atoms.

positional fluctuation of atom α-phosphate (PA) is larger (0.78 Å) and its RMS deviation from the initial position is ~1.6 Å at the end of the simulation. The observed abrupt changes in the PA RMS curve (Fig. 3 *C*) are due to transitions in the pyrophosphate dihedrals (Fig. 4 *B*). Thus, the PA position seems to be less stable. However, the PA atom forms interactions with important catalytic-site residues throughout the simulations, as we show below.

We next discuss the ligand interactions with protein residues and water molecules in the active site. The average distances between atoms participating in protein-ligand hydrogen bonds, along with the average hydrogen-bond lengths and occupancies are listed in Table 2. The time evolution of selected distances between pyrophosphate and protein atoms is plotted in Fig. 5.

In the crystal structures of RNase complexes with pyrophosphate-containing ligands (13,15,16), the ligand β-phosphate (PB) group interacts with the two catalytic histidines His^{12} and His^{119}, the proximal residues Gln^{11}, Phe^{120}, and a water molecule. In our simulations this group makes strong interactions with His^{12} and one or two water molecules, and somewhat weaker interactions with His^{119}, Phe^{120}, and Gln^{11}. In the first 2 ns, atom O1B interacts with His^{119} and Phe^{120} (see Fig. 5). Atom O2B forms a strong hydrogen bond with His^{12} and a weaker, direct or water-mediated interaction with Q11. At ≈2 ns, the pyrophosphate

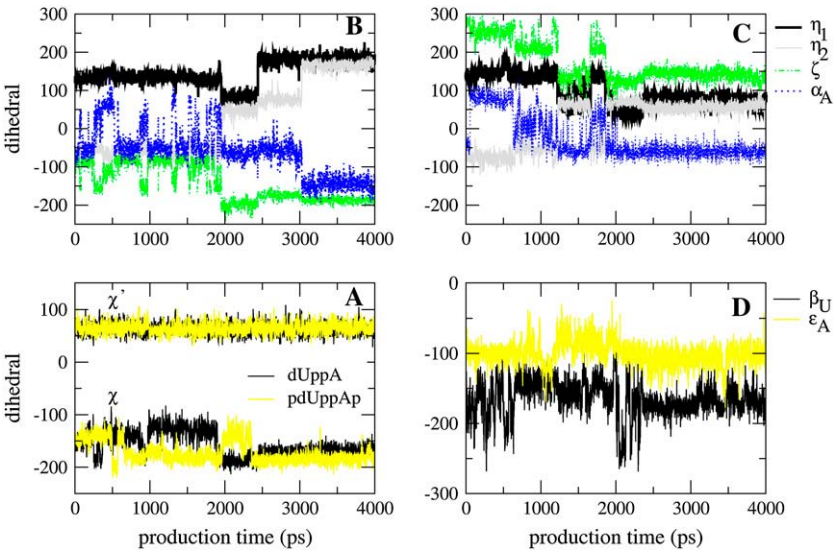

FIGURE 4 Time evolution of selected ligand dihedral angles in the simulations of the two complexes. The dihedral angles are defined in Fig. 2 and Table 1. (*A*) Dihedral angles χ' and χ. The black and yellow colors correspond, respectively, to the dUppA and pdUppA-3′-p ligand. (*B*) Ligand UppA pyrophosphate dihedral angles η_1, η_2, ζ, and α_A; (*C*) same as panel *B*, for ligand pdUppA-3′-p; and (*D*) terminal phosphate dihedrals β_U and ϵ_A of the ligand pdUppA-3′-p.

TABLE 1 Average values of selected ligand dihedral angles, observed in the simulations of the two complexes

Dihedral angle*	dUppA	X ray†	pdUppA-3′-p	X ray‡
Glycosyl dihedrals				
O4′U-C1′U-N1U-C2U(χ)	−135/−175§	−136	−182/−141	−130
O4′A-C1′A-N9A-4A(χ')	64	76	65	85
Phosphate dihedrals				
C4-C3-O3-PB(ϵ_U)	−173/91	176	−170	−82
C3-O3-PB-O3A(η_1)	80/133/180	121	69/142	106
O3-PB-O3A-PA(η_2)	−75/63/166	−82	−65/60	−71
PB-O3A-PA-O5′A(ζ)	−86/−179	−100	−102/−152/138	−95
O3A-PA-O5′-C5′(α_A)	−55/−145/49	−72	−57/79	−58
PA-O5′-C5′-C4′(β_A)	−173	−133	175	−136
PG-O3′-C3′-C4′(ϵ_A)			−100	−103
PD-O5′-C5′-C4′(β_U)			−165	−142
Backbone dihedrals				
O5′-C5′-C4′-C3′(γ_U)	−72/56	73	36/68	78
O5′-C5′-C4′-C3′(γ_A)	−48/41	51	−65/48	52
C5′-C4′-C3′-O3′(δ_U)	78/133	140	84/136	148
C5′-C4′-C3′-O3′(δ_A)	96	81	126	140

*The employed atom names and the corresponding dihedrals are shown in Fig. 2.
†From Leonidas et al. (15).
‡From Jardine et al. (16).
§For dihedrals which fluctuate in more than one basin (see Fig. 4), we compute separately and report the average value in each basin.

ζ dihedral angle undergoes a conformational transition (Fig. 4 *B*). Subsequently, O1B interacts with His^{12} and Phe^{120}; the Q11 interaction with both oxygens O1B and O2B is improved. The O1B and O2B atoms are also hydrogen-bonded to waters throughout the simulation (see Table 2). Atom O3 interacts with His^{119} in the last 1.5 ns.

The α-phosphate (PA) group interacts with residues Lys^7 and His^{119}. Atom O1A forms a strong hydrogen bond with Lys^7 in the first 3 ns. Atoms O2A and O3A interact with water molecules throughout the simulation and with His^{119} in the last 2 ns. For a brief period in the middle of the simulation, atom O2A makes an intramolecular hydrogen bond with O5 (not shown). A simulation structure of the active site region that is typical of the last 2-ns trajectory segment is shown in Fig. 6.

The His^{119} side chain can adopt two conformations A and B in the free RNase A, which differ by a rotation around the χ_1 angle (54). In the crystallographic structure of the complex, it is observed in conformation A (16). In the simulations it is retained in this conformation, with a mean χ_1 value of 152°. The His^{119} and adenine rings form continuous π–π stacking interactions, which presumably contribute to the stabilization of the His^{119} A orientation and the adenine ring syn orientation; the distance between the ring centers varies between ≈3.0 and 5.0 Å.

Residue Lys^{41} is located at a distance of 3.3 Å from atom O3 in the crystal structure. In the simulation, it forms water-mediated interactions with atoms O3 and the phosphate groups of the ligand, and a (noncontinuous) direct hydrogen bond for ~40% of the time with Gln^{11}. The positional fluctuation of its terminal NZ atom is 1.5 Å.

Thr^{45} confers to subsite B_1 of RNases the specificity for pyrimidine bases (2) by forming two hydrogen bonds with the uridine atoms N3U and O2U. In the simulations, both hydrogen bonds are almost continuously present (see Table 2). The uridine atom O4U forms indirect interactions with the Ser^{123} and the Asp^{83} side chains, mediated by one or two water molecules. Asp^{83} forms a second, continuous hydrogen bond with Thr^{45}. The uridine ring forms displaced stacking interactions with Phe^{120}. The adenine base forms two strong hydrogen bonds with Asn^{71} and weaker interactions with Gln^{69}. All these interactions are also observed in the crystal structure of the complex (16).

The ligand makes extensive interactions with the solvent (see Table 2). Each hydrogen-bonding atom of the ligand interacts with several hundred different water molecules in the course of the 4-ns simulation. The average (over all atoms) lifetime of these bonds is ≈2.3 ps; the largest average duration (5.9 ps) corresponds to water interactions with atom O2B.

Residues Arg^{10} (site P_2) and Lys^{66} (P_0) are located at distances >9 Å from the ligand phosphate groups and interact with water. Lys^{66} forms a salt bridge with Asp^{121} for ~0.5 ns. Its side chain undergoes frequent conformational transitions and the terminal NZ atom has a positional fluctuation of 2.9 Å. As we show below, this residue contributes to the stronger affinity of pdUppA-3′-p for RNase A.

Complex with pdUppA-3′-p

The time evolution of the Cartesian coordinates RMS deviation is shown in the right panel of Fig. 3. The simulation conformations remain close to the crystallographic structure. The total RMS deviation of the protein backbone heavy atoms (plot 3 *D*) and the ligand adenine and uracil rings (plot 3 *E*) converge to ≈0.6–0.7 Å at the end of the 4-ns production period, in close similarity with the behavior of dUppA complex. The glycosyl dihedral angles χ and χ' are maintained near the x-ray values (plot 4 *A*, *yellow curves*), indicating that the orientations of the two nucleotide rings are very stable. The β-phosphate (PB) group of the pyrophosphate linker occupies a stable position at the P_1 site, whereas the α-phosphate group (PA) is more mobile; the average positional fluctuations of the two phosphate atoms are, respectively, 0.41 Å and 0.81 Å. The pyrophosphate dihedrals η_1, η_2, ζ, and α_A undergo conformational transitions, as in the dUppA complex (Fig. 4 *C*). The two terminal 5′- and 3′-phosphate dihedrals β_U and ϵ_A (see Fig. 2) fluctuate mostly in a single basin (plot 4 *D*).

The average distances of atoms participating in ligand-protein hydrogen bonds, and the corresponding hydrogen-bond statistics are included in Table 2. The time evolution of selected distances is presented in Fig. 7. As in the dUppA complex, the β-phosphate group forms two strong hydrogen bonds with His^{12} and Phe^{120}, and three somewhat weaker

TABLE 2 Statistics of ligand-protein and ligand-water hydrogen bonds, observed in the simulations of the RNase A:dUppA and RNase A:pdUppA-3′-p complexes

	dUppA				pdUppA-3′-p			
	Distance		hb		Distance		hb	
Atom pair*	MD†	X ray	Length‡	Occupancy	MD†	X ray	Length‡	Occupancy
O1B-F120 (N)	3.4 (0.4)	3.2	2.9 (0.0)	52 (%)	3.0 (0.4)	2.9	3.0 (0.2)	82 (%)
O1B-H12 (NE2)	3.6 (0.1)		3.2 (0.1)	51	3.3 (0.9)		3.1 (0.2)	63
O1B-H119 (ND1)	3.5 (0.8)	3.1	2.7 (0.0)	44	3.5 (0.7)	2.8	2.6 (0.1)	28
O1B-water				25				
O2B-H12 (NE2)	3.5 (0.9)	2.8	2.7 (0.1)	49	3.4 (0.6)	2.4	2.7 (0.1)	37
O2B-K7 (NZ)					4.2 (1.7)		2.9 (0.2)	34
O2B-Q11 (NE2)	3.6 (0.6)	2.8	3.1 (0.1)	25	3.3 (0.5)	2.9	3.0 (0.2)	17
O2B-F120 (N)	4.6 (0.9)		3.2 (0.1)	8	4.8 (0.6)		3.2 (0.1)	2
O2B-water				138				100
				394§				**365**
O3-H119 (ND1)	3.9 (0.8)		3.0 (0.1)	29				
O3-Q11 (NE2)					3.8 (0.6)		3.3 (0.0)	15
O3-water				40				62
				70				**88**
O1A-K7 (NZ)	3.3 (0.9)		2.7 (0.1)	61	3.0 (0.7)	2.8	2.6 (0.0)	68
O1A-water				154				160
O2A-H119 (ND1)	4.2 (1.1)	3.0	3.0 (0.3)	28	3.3 (0.7)	3.4	3.2 (0.1)	58
O2A-water				198				148
O3A-H119 (ND1)	4.0 (0.8)		3.3 (0.1)	27	3.6 (0.8)		3.0 (0.2)	45
O3A-Q11 (NE2)	4.6 (0.8)		3.2 (0.1)	3	4.7 (0.8)		3.1 (0.2)	8
				484				**458**
O2D-K66 (NZ)					5.7 (2.4)		2.8 (0.1)	17
								17
O2G-K7 (NZ)					5.4 (2.1)		2.7 (0.1)	25
O3G-K7 (NZ)						2.7		
								25
N6A-N71 (OD1)	3.1 (0.4)	2.9	3.0 (0.3)	84	3.0 (0.2)	3.1	2.9 (0.2)	90
N6A-N67 (OD1)	3.6 (0.5)		3.0 (0.1)	21	3.8 (0.5)	3.3	3.2 (0.3)	17
				106				**109**
N7A-N71 (ND2)	3.1 (0.2)	2.9	3.1 (0.1)	91	3.1 (0.2)	3.2	3.1 (0.2)	92
N7A-water				14				25
				109				**120**
N1A-N67 (ND2)	3.3 (0.3)	3.1	3.0 (0.2)	26	3.3 (0.5)	3.4	3.2 (0.2)	33
N1A-water				37				44
				63				**77**
N3U-T45 (OG1)	2.9 (0.1)	2.9	2.8 (0.1)	100	2.8 (0.1)	2.8	2.8 (0.1)	100
				100				**100**
O2U-T45 (N)	3.0 (0.1)	2.8	3.0 (0.1)	83	3.0 (0.1)	2.8	3.0 (0.1)	89
				83				**89**
O4U-water				107				101

All distances in Å. The standard deviations are included in parentheses.

*The atomic names of the two ligands are indicated in Fig. 2.

†Average distance (with standard deviations in parentheses) between the corresponding heavy atoms in the entire 4-ns trajectory.

‡Average distance (with standard deviations in parentheses) in the portion of the 4-ns trajectory, where a hydrogen bond is formed. The criteria for the existence of a hydrogen bond employed here are 1), a maximum donor (D)-acceptor (A) distance of 3.4 Å; and 2), a minimum ∠ DHA of 120°.

§Total hydrogen-bond occupancy for each ligand group.

bonds with His^{119}, Gln^{11}, and Lys^{7}; the first four interactions are also present in the crystal structure (15). In the first 2 ns, atom O1B interacts with His^{119} and Phe^{120}, whereas O2B interacts with His^{12}. Both oxygens form hydrogen bonds with one or two water molecules, which sometimes bridge an interaction with Gln^{11}. The α-phosphate atoms O1A and O2A interact, respectively, with Lys^{7} and His^{119}; O3A interacts with Q11. A typical MD structure of the first 2-ns portion of the simulation is shown in Fig. 8. At $\approx$2 ns, the pyrophosphate ζ dihedral angle undergoes a conformational transition; subsequently, O1B interacts with His^{12}, Phe^{120}, and one or two waters, and O2B interacts with Lys^{7}, water, and Gln^{11}. The interaction between the α-phosphate (atoms O2A, O3A) and His^{119} is also improved.

Residue Lys^{41} forms a hydrogen bond with the ligand O3 atom in complex I of the crystallographic unit cell, with a

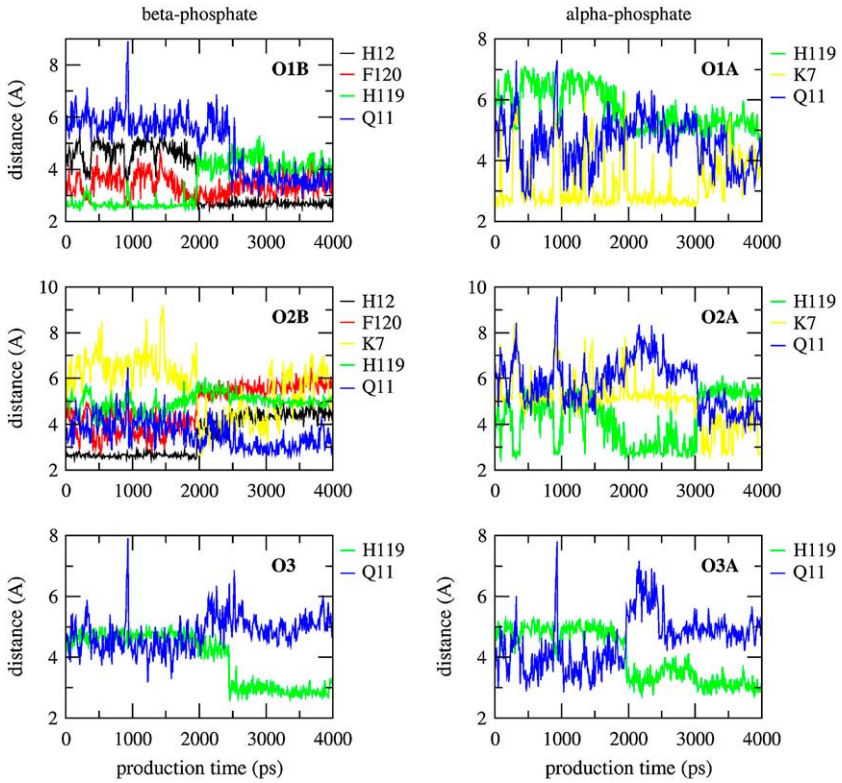

FIGURE 5 Time evolution of selected dUppA-protein distances in the 4-ns production-phase simulation.

length of 3.1 Å. In the simulations this hydrogen bond is observed in the first ≈500 ps (Fig. 7). Subsequently, Lys[41] forms water-mediated interactions with the two pyrophosphate groups as in the dUppA complex; the positional fluctuation of its terminal NZ atom is 1.5 Å.

Residue Lys[7] forms two hydrogen bonds with the PA and PG groups, with respective occupancies 70% and 25% (Table 2). This behavior is in accord with the crystallographic structure, where Lys[7] hydrogen-bonds to O1A in one of the two complexes in the crystallographic unit cell and to O3G in the second complex (15). The His[119] ring is maintained in conformation A with an average χ_1 angle of 153°, and forms continuous π–π stacking interactions with the adenine ring, as in the dUppA complex. Both residues contribute to the higher relative affinity of pdUppA-3′-p (see below).

The uridine and adenosine moieties of pdUppA-3′-p interact, respectively, with Thr[45] and Asn[71] via two strong hydrogen

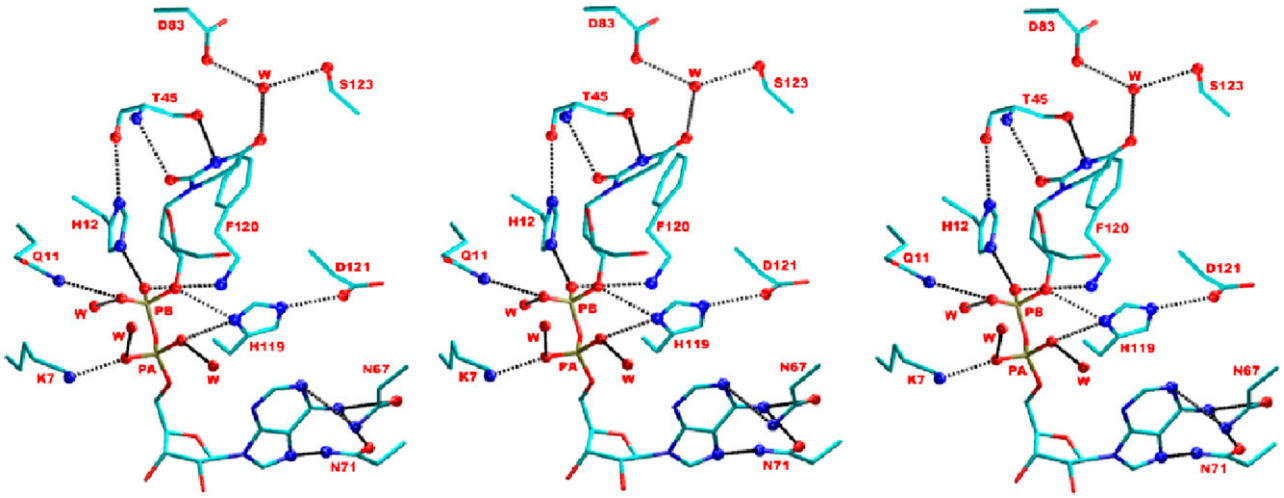

FIGURE 6 Wall (*left*) and cross (*right*) stereo representations of a typical structure of the dUppA-complex active site, observed in the second 2-ns simulation segment. The important interactions of dUppA with surrounding protein residues and waters are indicated.

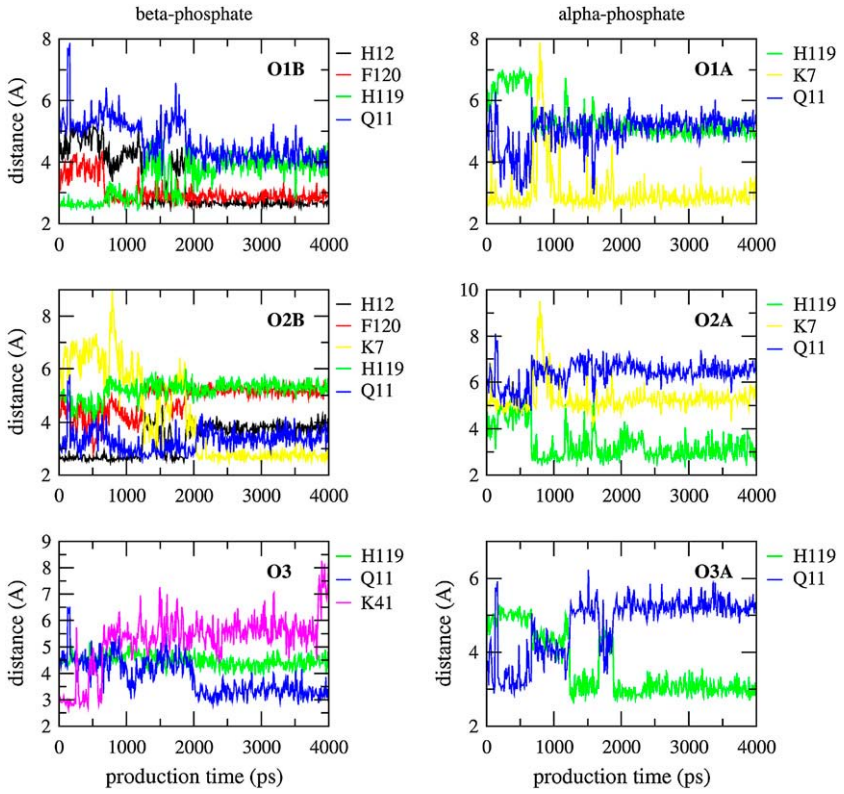

FIGURE 7 Time evolution of selected pdUppA-3′-p-protein distances in the 4-ns production-phase simulation.

bonds. The uridine ring makes off-centered stacking interactions with the Phe[120] ring. The adenine moiety interacts also with Asn[67] and Gln[69]. Ser[123] often makes water-mediated interactions with O4U and Asp[83]. Arg[10] is more remote (site P_2) and interacts mostly with water. All these interactions are in close agreement with the crystal structure (15) and similar to what was observed in the simulations of the dUppA complex.

The 5′ (PD) terminal phosphate interacts with water molecules throughout the run. In ≈75% of the simulation length it makes an intramolecular hydrogen bond with the oxygen O2A of the α-phosphate (not shown). In the last ns it also interacts on and off with Lys[66] of subsite P_0. This lysine interacts also with solvent molecules throughout the simulation. The positional fluctuation of the Lys[66] NZ atom is 3.2 Å, slightly larger than in the dUppA complex (2.9 Å). In the crystal structure, the position of the same atom is well defined in molecule I and its distance from the nearest oxygen of the PD phosphate is ≈4.7 Å. In molecule II of the

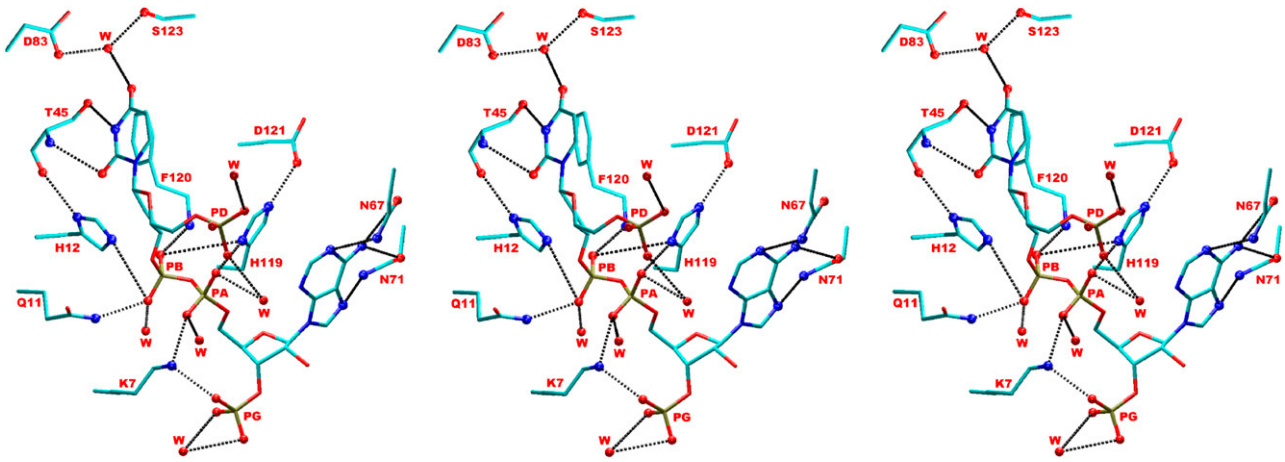

FIGURE 8 Wall (*left*) and cross (*right*) stereo representations of a typical structure of the pdUppA-3′-p -complex active site, observed in the first 2-ns simulation segment. The important interactions of dUppA with surrounding protein residues and waters are indicated.

unit cell there is no density beyond the C_β atom, suggesting that Lys^{66} is flexible. Even though Lys^{66} does not make strong interactions with the ligand, its contribution in the higher stability of the dUppA-3′-p complex is significant, as we show in the next section.

As in the dUppA complex, the pdUppa-3′-p ligand makes numerous hydrogen-bonding interactions with the solvent (see Table 2). Atom O2B hydrogen-bonds with 11 different waters and forms the longest-living interactions (with average lifetime of 16.1 ps). Other ligand atoms interact typically with several hundred different water molecules; when averaged over all ligand atoms, the mean water-ligand hydrogen bond lifetime is 3.1 ps.

Poisson-Boltzmann electrostatic association free energies

Based on the experimental K_i values of the pdUppA-3′-p and dUppA ligands (27 nM and 11.3 μM), the pdUppA-3′-p complex is estimated to be more stable by −3.6 kcal/mol. The net charge of the two ligands is −4 (pdUppA-3′-p) and −2 (dUppA); that of RNase is +8 at the experimental pH 5.5 of the solution (15,16). Thus, electrostatic interactions are expected to be the most important factor affecting the stability of the two complexes.

The electrostatic association free energies of the two complexes can be calculated by a Poisson-Boltzmann model (34–37). Furthermore, a component analysis (38,39) can identify which protein or ligand groups contribute mostly to the total free energy, and provide a better understanding of the differences between the two complexes.

The total Poisson-Boltzmann binding free energies for the two complexes are included in Table 3. To increase accuracy (39,51,55), the results were averaged over 200 snapshots, spanning the 4 ns simulations. The ionic strength of the solution corresponded to the experimental value of 0.2 M monovalent ion concentration. Additional calculations were performed at 0 M, to investigate the dependence of the results on the ionic concentration.

TABLE 3 Total electrostatic binding energies for the two complexes (kcal/mol)

	dUppA		pdUppA-3′-p		$\Delta\Delta G_{bind}$	
ϵ_p	0 M	0.2 M	0 M	0.2 M	0 M	0.2 M
2	−17.5 (4.0)	−14.1 (4.0)	−28.1 (3.5)	−22.0 (3.3)	−10.6	−7.9
4	−14.3 (2.0)	−11.0 (2.0)	−22.1 (2.1)	−16.1 (2.0)	−7.8	−5.1
8	−12.3 (1.0)	−9.1 (1.0)	−18.7 (1.4)	−12.8 (1.3)	−6.4	−3.7
16	−10.9 (0.5)	−7.8 (0.5)	−16.6 (1.0)	−10.7 (0.9)	−5.7	−2.9
20	−10.4 (0.4)	−7.4 (0.4)	−16.0 (0.9)	−10.2 (0.8)	−5.6	−2.8

Averages over 200 conformations spanning the 4 ns simulations. Values are calculated with a water dielectric constant of 80 and a protein/ligand constant of ϵ_p. The uncertainty (in parentheses) is computed as the standard deviation of averages, which are obtained by partitioning the 4 ns trajectory into four groups of 1 ns. The ionic strength of the experimental binding measurements is 0.2 M.

The binding free energies of both complexes are negative, implying that the electrostatic interactions promote association. The pdUppA-3′-p complex is more stable by 7.9 kcal/mol ($\epsilon_p = 2$) to 2.8 ($\epsilon_p = 20$) kcal/mol at the experimental (0.2 M) ionic strength. Thus, the PB results are in good agreement with the experimental value of 3.6 kcal/mol for $\epsilon_p > 2$; notably, the experimental value is exactly reproduced with a dielectric constant $\epsilon_p = 8$.

At 0 M, the association free energies are somewhat more negative. This increase in the affinity of oligonucleotide ligands for RNase A at low salt concentrations has been established experimentally (56,57).

Poisson-Boltzmann free energy component analysis

The relative electrostatic binding free energy obtained by PB is in good agreement with experiment. To gain insight on the interactions that increase the affinity of pdUppA-3′-p, we separate the total electrostatic free energy of both complexes into interaction and desolvation components. The interpretation of these components was presented in Theory and Methods. For a detailed discussion, see Archontis et al. (39).

The results are included in Table 4. The interaction term ΔG^{PL}_{int} is related to the direct electrostatic interaction energy between protein and ligand charges in the solvated complex. For both complexes it is negative, reflecting the fact that the direct electrostatic interactions between protein and ligand charges favor association. Its (absolute) value is larger in the pdUppa-3′-p complex (−70.0 kcal/mol compared to −54.1 kcal/mol) due to the higher charge of this inhibitor.

The protein and ligand desolvation terms are related to the change in the interaction of the protein (or ligand) with the polarization charge of the surrounding medium, upon binding. Both terms are positive, reflecting the fact that the protein and ligand interact more strongly with the induced charge in their unbound state, where they are surrounded by the high-dielectric solvent. The protein desolvation component is somewhat more positive for the large inhibitor, in accord

TABLE 4 Decomposition of the total electrostatic free-energies of Table 3 into interaction and desolvation components (kcal/mol)

	dUppA	pdUppA-3′-p	$\Delta\Delta G$
ΔG^{PL}_{inter}	−54.0 (2.1)	−70.0 (3.7)	−15.9
ΔG^{P}_{desolv}	20.0 (0.6)	22.7 (0.8)	2.7
ΔG^{L}_{desolv}	23.0 (0.6)	31.2 (1.1)	8.2
Total*	−11.0 (4.5)	−16.1 (5.4)	−5.1

The various components were explained in Theory and Methods. Values correspond to a protein/ligand dielectric constant of 4 and an ionic strength of 0.2 M. The uncertainty (in parentheses) is computed as the standard deviation of averages, which are obtained by partitioning the 4 ns trajectory into four groups of 1 ns.
*The total values are taken from Table 3.

with the larger reduction in the solvent-accessible surface area of RNase A in the simulations of the pdUppA-3′-p complex (418 Å^2, compared to 372 Å^2 in the dUppA complex, evaluated by the Lee-Richards algorithm with a probe radius of 1.4 Å). The ligand desolvation component is significantly more positive for pdUppA-3′-p (31.2 kcal/mol, compared to 23.0 kcal/mol). This can be attributed to the additional two phosphate groups, which increase the total interaction between pdUppA-3′-p and the induced charge at the ligand-solvent interface. The reduction in the solvent-accessible surface area of pdUppA-3′-p in the simulations is 664 Å^2, compared to 624 Å^2 for dUppA.

From the above analysis it follows that the increased relative stability of the pdUppA-3′-p complex originates mainly from enhanced electrostatic interactions between the pdUppA-3′-p ligand and the protein, reflected by the more negative component $\Delta G_{\text{int}}^{\text{PL}}$. Insight on the protein residues, which mostly contribute to the increased affinity of pdUppA-3′-p, can be obtained by further decomposing the term $\Delta G_{\text{int}}^{\text{PL}}$ into residue contributions. The largest values are included in Table 5. The meaning of these components is further analyzed in the next section and in Archontis et al. (39).

The most important contributions are due to residues Lys^7, His^{119}, and Lys^{66}. In Table 6 we decompose further these residue terms into contributions from interactions with various ligand moieties. Lys^7 forms stronger interactions with the pyrophosphate group and the 3′-end moiety of pdUppa-3′-p, which contains the γ-phosphate. This is in accord with the hydrogen-bond analysis presented above. Residue Lys^7 makes 1.27 hydrogen bonds (per frame) with the atoms O1A, O2B, and O2G of pdUppA-3′-p, compared to 0.61 hydrogen bonds with atom O1A in dUppa. The next most important residues His^{119} and Lys^{66} interact more strongly with the 5′-end (δ-phosphate) and to a lesser extent with the intermediate pyrophosphate group of pdUppa-3′-p. His^{119} forms, respectively, 1.31 and 1.28 hydrogen bonds (per frame) with the pyrophosphate atoms O1B, O3, O2A, O2B of ligands pdUppA-3′-p and dUppA; the average H119(Nδ1)–O3A distance is somewhat smaller (3.0 Å, compared to 3.3 Å) in the pdUppA-3′-p complex, possibly contributing to a stronger interaction.

TABLE 5 Contributions from selected residues to the protein-ligand interaction component $\Delta G_{\text{inter}}^{\text{PL}}$ (kcal/mol)

Residue	dUppA	pdUppA-3′-p	$\Delta\Delta G_{\text{inter}}^{\text{R}}$
Lys^7	−9.3 (0.6)	−17.9 (1.1)	−8.6
His^{119}	−18.4 (0.3)	−25.4 (0.6)	−7.0
Lys^{66}	−0.8 (0.4)	−4.3 (0.4)	−3.5
His^{12}	−19.6 (0.1)	−21.0 (0.0)	−1.3
Lys^{41}	−5.2 (0.6)	−5.5 (1.9)	−0.2
Asp^{121}	2.8 (0.1)	5.9 (0.3)	3.1
Total*	−54.1 (2.1)	−70.0 (3.7)	−16.1

Values are calculated with a protein/ligand dielectric constant of 4 and ionic strength of 0.2 M. The uncertainty (in parentheses) is computed as the standard deviation of averages, which are obtained by partitioning the 4 ns trajectory into 4 groups of 1 ns.

*Total value, listed in the first row of Table 4.

TABLE 6 Decomposition of the residue-ligand relative interaction free energies of Table 5 (term $\Delta\Delta G_{\text{inter}}^{\text{R}}$) into contributions from ligand moieties (kcal/mol)

Ligand moiety	Lys^7	His^{119}	Lys^{66}	His^{12}	Lys^{41}
5′-end*	−0.5	−4.1	−2.7	−0.9	−0.7
Pyrophosphate†	−5.3	−1.7	−0.7	−0.1	0.8
3′-end‡	−2.9	−0.9	−0.1	−0.6	−0.3
Total§	−8.6	−7.0	−3.5	−1.4	−0.3

All values are relative to the dUppA complex and correspond to a protein/ligand dielectric constant of 4, a solvent dielectric constant of 80 and an ionic strength of 0.2 M.

*The 5′-end includes atoms H5T, O5, C5, HC51, HC52 (ligand dUppA) and H5T, O3D, PD, O1D, O2D, O5, C5, HC51, HC52 (ligand pdUppA-3′-p) (see Fig. 2).

†The pyrophosphate moiety includes atoms C3, HC3, O3, PB, O1B, O2B, O3A, PA, O1A, O2A, O5′, C5′, HC5′1, HC5′2 for both ligands.

‡The 3′-end moiety includes atoms C3′, HC3′, O3′, H3′ (ligand dUppA) and C3′, HC3′, O3′, PG, O1G, O2G, O3G, H3T (ligand pdUppA-3′-p).

§Total value, listed in the last column of Table 5.

DISCUSSION AND CONCLUSIONS

The Coulombic forces exerted by various RNase A subsites on RNA analog substrates have been investigated by mutagenesis experiments. According to these studies, Lys^{66} (site P_0) and the pair Lys^7/Arg^{10} (site P_2) contribute, respectively, 0.9 kcal/mol and 1.2 kcal/mol to the binding of fluorescein-dAUAA (56) at a pH of 6.0; His^{12} and His^{119} (site P_1) contribute 1.4 kcal/mol and 1.1 kcal/mol to the binding of 3′-UMP at the same pH (58). These values are much smaller than the corresponding residue free-energy components $\Delta G_{\text{int}}^{\text{PL}}$ (Table 5). However, it should be noted that a PB interaction free-energy component associated with residue *R* (as the ones reported in Table 5) does not correspond quantitatively to the total free energy change of the complex due to neutralization of *R* (even though it does provide a qualitative measure of the R contribution to the total binding affinity). Two other factors are likely to partly compensate for this interaction free-energy component, yielding a smaller total free-energy change. First, the neutralization of *R* changes the polarization charge that is induced at the entire protein/solvent interface (dissociated state) or complex/solvent interface (bound complex state), modifying thereby the total protein desolvation free-energy component. Furthermore, the charge perturbation on *R* could cause structural relaxation in the complex, which might perturb the interaction components of other residues and change the total protein or ligand desolvation components. A detailed discussion of the connection between the PB free-energy components and mutagenesis, and specific numerical examples for complexes of the protein aspartyl-tRNA synthetase, are presented in Archontis et al. (39).

In addition to the electrostatic free energies computed here, the total absolute binding free energies contain contributions from other factors, such as the nonpolar interactions, the translational, conformational and vibrational entropy loss of the ligand and protein, and the entropy gain due to the release of water molecules (23,28–33,59–61).

An estimate of the nonpolar contribution to the relative binding affinity can be obtained by a standard surface model (62). Given that the average reduction in the total solvent-accessible surface area of the pdUppA-3′-p and dUppA complexes in the simulations is 1082 Å^2 and 996 Å^2, respectively, the model yields an additional stabilization of the pdUppA-3′-p complex by ≈0.5 kcal/mol.

Contributions from ligand/protein entropic terms could also be estimated by various approximate methods (23,28–33,59–61). For example, the two additional dihedral angles of pdUppA-3-′p, PD-O5′-C5′-C4′(β_U), and PG-O3′-C3′-C4′(ϵ_A), fluctuate in a single minimum throughout the 4-ns simulations (see Table 1 and Fig. 4 *D*). Assuming an average loss of entropy per rotatable bond of 0.4–0.5 kcal/mol (31,63), the restriction of these angles upon association destabilizes the pdUppA-3-′p complex by ≈0.8–1.0 kcal/mol, with respect to dUppA. Additional contributions due to the ligand translational/rotational and the protein side-chain entropy are likely to cancel approximately in the relative free energy difference, because the two ligands are similar, bind at the same position/orientation in the complex and have similar positional fluctuations in the simulations. We thus do not compute them here.

Other factors that could introduce inaccuracies in the continuum model are the use of charges/radii optimized for molecular mechanics calculations and the use of uniform dielectric constants for the protein/ligand and solvent, despite the contrary evidence from simulations (37,64–68). Furthermore, the protein and ligand structures are assumed identical in the complex and the dissociated states in our calculations. The structural fluctuations of the complex are taken into account by averaging the results over the 4-ns trajectories, but any protein/ligand relaxation upon dissociation is only implicitly taken into account via the dielectric constant (36,55,69–71). Given these approximations and the appreciable ligand sizes (68 and 73 atoms), it is noteworthy that our continuum model yields relative binding free energies in excellent agreement with experiment for $\epsilon_p = 8$, and fair agreement in the entire range $\epsilon_p = 2$–20.

Ligand-design methods based on PB calculations of single (e.g., energy-minimized) conformations may be successful in ranking a family of complexes, provided their docking/energy minimization protocols produce representative conformations. An example of such a high-throughput docking/continuum electrostatics method, which discovered a set of β-secretase inhibitors, is presented in Huang et al. (25). In the case of the two RNase A complexes considered here, the x-ray conformations are indeed sufficient for the accurate evaluation of the relative binding affinity; PB calculations with the x-ray structures yield a result of −5.3 kcal/mol in favor of the pdUppa-3′-p ligand (with a protein/ligand dielectric constant $\epsilon_p = 4$ and an ionic strength of 0.2 M), in perfect agreement with the corresponding simulation average (−5.1 kcal/mol; see Table 3). On the other hand, MD simulations are likely to provide more representative structures in some systems, e.g., when a ligand or protein mutation is associated with structural relaxation (26,39). The computational requirements of such MD-based ligand design methods may be reduced by using a more approximate free-energy scoring function, such as in the linear interaction energy approach (20,26).

In conclusion, in this work we have studied by molecular dynamics simulations and Poisson-Boltzmann calculations the complexes between RNase A and the two dinucleotide inhibitors dUppA and pdUppa-3′-p. The simulations reproduce structural features which are characteristic of complexes between RNases and pyrophosphate-containing nucleotidic inhibitors (13–17); in particular, the β-phosphate group of each ligand interacts with the P_1 site residues His^{12} and His^{119}, Gln^{11}, and Phe^{120} (Table 2), in agreement with the crystal structures (15,16). The β-phosphate position is very stable, with an RMS deviation from the crystal structure of 0.6 Å at the end of the 4.4 ns simulation (Fig. 3) and an overall positional (RMS) fluctuation of 0.41–0.45 Å. The interaction with His^{12}, which is persistent throughout the simulations, presumably contributes to the stability. The α-phosphates are more mobile, with a positional fluctuation of 0.78–0.81 Å, and interact mainly with Lys^7 and His^{119}. The syn orientation of the adenosine ring, which characterizes RNase complexes with pyrophosphate-containing ligands, is maintained throughout the simulations; it is stabilized in part by stacking interactions with His^{119}. The direct and water-mediated hydrogen-bonding interactions of the two bases with the RNase catalytic-site residues are well reproduced.

Continuum electrostatics calculations predict that the pdUppa-3′-p ligand binds to RNase A with a relative affinity that ranges between −7.9 kcal/mol (protein/ligand dielectric $\epsilon_p = 2$) and −2.8 kcal/mol ($\epsilon_p = 20$). The experimental relative value, −3.7 kcal/mol, is reproduced with an $\epsilon_p = 8$. The good agreement of the continuum model with the experimental relative affinities suggests that the electrostatic interactions are mainly responsible for the different stability of the two complexes.

The present computational study provides further insight into the remarkable differences in potency of the two inhibitors, which complements efficiently the previous crystallographic results (15,16). A free-energy decomposition shows that the increased affinity of RNase for the pdUppa-3′-p ligand is mainly due to interactions with Lys^7, His^{119}, and Lys^{66} (Table 5). The interactions of Lys^7 and Lys^{66}, respectively, with the 3′ and 5′ phosphate groups and the stabilizing role of these two groups in the overall conformation of pdUppA-3′-p, both inferred from the present study and from the crystal structures (15,16), seem to be the main

reason for the differences in the potency of the two inhibitors.

This work has been partly supported by a ''Joined Research and Technology Grant'' between Cyprus and Greece (to G.A., D.L., and N.G.O.), and PENEK grants for the ''Research Integration of Young Cypriot Researchers'' and the ''Research Reinforcement of Young Cypriot Researchers'' (to G.A. and S.P.).

All calculations were performed on a Linux cluster of the Biophysics group at the University of Cyprus.

REFERENCES

1. Cho, S., J. J. Bentema, and J. Zhang. 2005. The ribonuclease A superfamily of mammals and birds: identifying new members and tracing evolutionary histories. *Genomics*. 85:208–220.
2. Raines, R. T. 1998. Ribonuclease A. *Chem. Rev*. 98:1045–1065.
3. Riordan, J. F. 2001. Angiogenin. *Methods Enzymol*. 341:263–273.
4. Fett, J. W., D. J. Strydom, R. R. Lobb, E. Alderman, J. L. Bethune, J. F. Riordan, and B. L. Vallee. 1985. Isolation and characterization of angiogenin, an angiogenic protein from human carcinoma cells. *Biochemistry*. 24:5480–5486.
5. Gleich, G., and C. R. Adolphson. 1986. The eosinophilic leukocyte: structure and function. *Adv. Immunol*. 39:177–253.
6. Vescia, S., D. Tramontano, G. Augusti-Tocco, and G. D. Alessio. 1980. In vitro studies on selective inhibition of tumor cell growth by seminal ribonuclease. *Cancer Res*. 40:3740–3744.
7. Rosenberg, H. F., and J. B. Domachowske. 2001. Eosinophils, eosinophil ribonucleases and their role in host defense against respiratory virus pathogens. *J. Leukoc. Biol*. 70:691–698.
8. Boix, E. 2001. Eosinophil cationic protein. *Methods Enzymol*. 341: 287–305.
9. Lopez, X., D. M. York, A. Dejaegere, and M. Karplus. 2002. Theoretical studies on the hydrolysis of phosphate diesters in the gas phase, solution and RNase A. *Int. J. Quantum Chem*. 86:10–26.
10. McPherson, A., G. Brayer, and R. D. Morrison. 1986. Crystal structure of RNase A complexed with $d(pA)_4$. *J. Mol. Biol*. 189:305–327.
11. Zegers, I., D. Maes, M.-H. Dao-Thi, F. Poortmans, R. Palmer, and L. Wyns. 1994. The structures of RNase A complexed with 3′-CMP and dCpA: active site conformation and conserved water molecules. *Protein Sci*. 3:2322–2339.
12. Toiron, C., C. Gonzalez, M. Bruix, and M. Rico. 1996. Three-dimensional structure of the complexes of ribonuclease A with 2′,5′-CpA and 3′,5′-CpA in aqueous solution, as obtained by NMR and restrained molecular dynamics. *Protein Sci*. 5:1633–1647.
13. Leonidas, D. D., R. Shapiro, L. I. Irons, N. Russo, and K. R. Acharya. 1997. Crystal structures of ribonuclease A complexes with 5′-diphosphoadenosine 3′-phosphate and 5′-diphosphoadenosine 2′-phosphate at 1.7 Å resolution. *Biochemistry*. 36:5578–5588.
14. Russo, N., and R. Shapiro. 1999. Potent inhibition of ribonuclease A by 3′,5′- pyrophosphate-linked nucleotides. *J. Biochem*. (*Tokyo*). 274: 14902–14908.
15. Leonidas, D. D., R. Shapiro, L. I. Irons, N. Russo, and K. R. Acharya. 1999. Toward rational design of Ribonuclease inhibitors: high resolution structure of a ribonuclease A complex with a potent 3′,5′-pyrophosphate-linked dinucleotide inhibitor. *Biochemistry*. 38:10287–10297.
16. Jardine, A. M., D. D. Leonidas, J. L. Jenkins, C. Park, R. T. Raines, K. R. Acharya, and R. Shapiro. 2001. Cleavage of 3′,5′-pyrophosphate-linked dinucleotides by ribonuclease A and angiogenin. *Biochemistry*. 40:10262–10272.
17. Leonidas, D. D., G. B. Chavali, N. G. Oikonomakos, E. D. Chrysina, M. N. Kosmopoulou, M. Vlassi, C. Franking, and K. R. Acharya. 2003. High resolution crystal structures of ribonuclease A with adenylic and uridylic nucleotide inhibitors. Implications for structure-based design of ribonucleolytic inhibitors. *Protein Sci*. 12:2559–2574.
18. Hatzopoulos, G. N., D. D. Leonidas, R. Kardakaris, J. Kobe, and N. G. Oikonomakos. 2005. The binding of IMP to Ribonuclease A. *FEBS J*. 272:3988–4001.
19. Massova, I., and P. Kollman. 1999. Computational alanine-scanning to probe protein-protein interactions: a novel approach to evaluate binding free energies. *J. Am. Chem. Soc*. 121:8133–8143.
20. Aqvist, J., V. B. Luzhkov, and B. O. Brandsal. 2002. Ligand binding affinities from MD simulations. *Acc. Chem. Res*. 35:358–365.
21. Simonson, T., G. Archontis, and M. Karplus. 2002. Free-energy simulations come of age: protein-ligand recognition. *Acc. Chem. Res*. 35: 430–437.
22. Gouda, H., I. D. Kuntz, D. A. Case, and P. A. Kollman. 2003. Free energy calculations for theophylline binding to an RNA aptamer: comparison of MM-PBSA and thermodynamic integration methods. *Biopolymers*. 68:16–34.
23. Swanson, J. M. J., R. H. Henchman, and J. A. McCammon. 2004. Revisiting free energy calculations: a theoretical connection to MM/PBSA and direct calculation of the association free energy. *Biophys. J*. 86:67–74.
24. Archontis, G., K. A. Watson, Q. Xie, G. Andreou, E. Chrysina, S. E. Zographos, N. G. Oikonomakos, and M. Karplus. 2005. Glycogen phosphorylase inhibitors: a free energy perturbation analysis of glucopyranose spirohydantoin analogues. *Proteins Struct. Funct. Bioinf*. 61: 984–998.
25. Huang, D., U. Luthi, P. Kolb, K. Elder, M. Cecchini, S. Audetat, A. Barberis, and A. Caflisch. 2005. Discovery of cell-permeable non-peptide inhibitors of β-secretase by high-throughput docking and continuum electrostatics calculations. *J. Medicin. Chem*. 48:5108–5111.
26. Ersmark, K., M. Nervall, E. Hamelink, L. K. Janka, J. C. Clemente, B. M. Dunn, M. J. Blackman, B. Samuelsson, J. Aqvist, and A. Hallberg. 2005. Synthesis of malarial plasmepsin inhibitors and prediction of binding modes by molecular dynamics simulations. *J. Medicin. Chem*. 48:6090–6106.
27. Straatsma, T., and J. A. McCammon. 1991. Theoretical calculations of relative affinities of binding. *Methods Enzymol*. 202:497–511.
28. Hermans, J., and L. Wang. 1997. Inclusion of loss of translational and rotational freedom in theoretical estimates of free energies of binding: application to a complex of benzene and mutant T4 lysozyme. *J. Am. Chem. Soc*. 119:2707–2714.
29. Luo, R., and M. K. Gilson. 2000. Synthetic adenine receptors: direct calculation of binding affinity and entropy. *J. Am. Chem. Soc*. 122: 2934–2937.
30. Luo, H., and K. Sharp. 2002. On the calculation of absolute macromolecular binding free energies. *Proc. Natl. Acad. Sci. USA*. 99:10399–10404.
31. Lazaridis, T., A. Masunov, and F. Gandolfo. 2002. Contributions to the binding free energy of ligands to avidin and streptavidin. *Proteins Struct. Funct. Bioinf*. 47:194–208.
32. Boresch, S., F. Tettinger, M. Leitgeb, and M. Karplus. 2003. Absolute binding free energies: a quantitative approach for their calculation. *J. Phys. Chem. B*. 107:9535–9551.
33. Woo, H.-J., and B. Roux. 2005. Calculation of absolute protein-ligand binding free energy from computer simulations. *Proc. Natl. Acad. Sci. USA*. 102:6825–6830.
34. Gilson, M. K., and B. H. Honig. 1987. Calculation of electrostatic potentials in an enzyme active site. *Nature*. 330:84–86.
35. Honig, B., and A. Nicholls. 1995. Classical electrostatics in biology and chemistry. *Science*. 268:1144–1149.
36. Warshel, A., and A. Papazyan. 1998. Electrostatic effects in macromolecules: fundamental concepts and practical modeling. *Curr. Opin. Struct. Biol*. 8:211–217.
37. Simonson, T. 2003. Electrostatics and dynamics of proteins. *Rep. Prog. Phys*. 66:737–787.

38. Hendsch, Z., and B. Tidor. 1999. Electrostatic interactions in the GCN4 leucine zipper: substantial contributions arise from intramolecular interactions enhanced on binding. *Protein Sci.* 8:1381–1392.

39. Archontis, G., T. Simonson, and M. Karplus. 2001. Binding free energies and free energy components from molecular dynamics and Poisson-Boltzmann calculations; application to amino acid recognition by aspartyl-tRNA synthetase. *J. Mol. Biol.* 306:307–327.

40. Mackerell, D. A., D. Bashford, M. Bellott, R. Dunbrack, J. Evanseck, M. Field, S. Fischer, J. Gao, H. Guo, S. Ha, D. Joseph, L. Kuchnir, K. Kuczera, F. Lau, C. Mattos, S. Michnick, T. Ngo, D. Nguyen, B. Prodhom, W. Reiher, B. Roux, J. Smith, R. Stote, J. Straub, M. Watanabe, J. Wiorkewicz-Kuczera, D. Yin, and M. Karplus. 1998. An all-atom empirical potential for molecular modeling and dynamics study of proteins. *J. Phys. Chem. B.* 102:3586–3616.

41. Jorgensen, W. L., J. Chandrasekhar, J. D. Madura, R. W. Impey, and M. L. Klein. 1983. Comparison of simple potential functions for simulating liquid water. *J. Chem. Phys.* 79:926–935.

42. Stote, R., D. States, and M. Karplus. 1991. On the treatment of electrostatic interactions in biomolecular simulation. *J. Chem. Phys.* 88:2419–2433.

43. Brooks, III, C. L., and M. Karplus. 1983. Deformable stochastic boundaries in molecular dynamics. *J. Chem. Phys.* 79:6312–6325.

44. Brooks, III, C. L., A. T. Brünger, and M. Karplus. 1985. Active site dynamics in protein molecules: a stochastic boundary molecular-dynamics approach. *Biopolymers.* 24:843–865.

45. Ryckaert, J. P., G. Ciccotti, and H. J. C. Berendsen. 1977. Numerical integration of the Cartesian equations of motion of a system with constraints: molecular dynamics of *n*-alkanes. *J. Comput. Phys.* 23:327–341.

46. Simonson, T., G. Archontis, and M. Karplus. 1997. Continuum treatment of long-range interactions in free energy calculations. application to protein-ligand binding. *J. Phys. Chem. B.* 101:8349–8362.

47. Archontis, G., T. Simonson, D. Moras, and M. Karplus. 1998. Specific amino acid recognition by aspartyl-tRNA synthetase studied by free energy simulations. *J. Mol. Biol.* 275:823–846.

48. Archontis, G., and T. Simonson. 2001. Dielectric relaxation in an enzyme active site: molecular dynamics simulations interpreted with a macroscopic continuum model. *J. Am. Chem. Soc.* 123:11047–11056.

49. Brooks, B. R., R. E. Bruccoleri, B. D. Olafson, D. J. States, S. Swaminathan, and M. Karplus. 1983. CHARMM: a program for macromolecular energy, minimization, and dynamics calculations. *J. Comput. Chem.* 4:187–217.

50. Gilson, M. K., and B. H. Honig. 1988. Calculating the electrostatic potential of molecules in solution: method and error assessment. *J. Comput. Chem.* 9:327–335.

51. van Vlijmen, H. W., M. Schaefer, and M. Karplus. 1998. Improving the accuracy of protein pKa calculations: conformational averaging versus the average structure. *Proteins Struct. Funct. Bioinf.* 33:145–158.

52. Madura, J., J. Briggs, R. Wade, M. Davis, B. Luty, A. Ilin, J. Antosiewicz, M. Gilson, B. Baheri, L. Scott, and J. McCammon. 1995. Electrostatics and diffusion of molecules in solution: simulations with the University of Houston Brownian Dynamics Program. *Comput. Phys. Comm.* 91:57–95.

53. Landau, L., and E. Lifschitz. 1980. Electrodynamics of Continuous Media. Pergamon Press, New York, NY.

54. Leonidas, D. D., T. K. Maiti, A. Samanta, S. Dasgupta, T. Pathak, S. E. Zographos, and N. G. Oikonomakos. 2006. The binding of 3-′-*n*-piperidine-4-carboxyl-3′-deoxy-ara-uridine to ribonuclease A in the crystal. *Bioorg. Med. Chem.* In press.

55. Archontis, G., and T. Simonson. 2005. Proton binding to proteins: a free energy component analysis using a dielectric continuum model. *Biophys. J.* 88:3888–3904.

56. Fisher, B. M., J.-H. Ma, and R. T. Raines. 1998. Coulombic forces in protein-RNA interactions: binding and cleavage by ribonuclease A and variants at Lys^{7}, Arg^{10} and Lys^{66}. *Biochemistry.* 37:12121–12132.

57. Fisher, B. M., L. W. Schultz, and R. T. Raines. 1998. Coulombic effects of remote subsites on the active site of ribonuclease A. *Biochemistry.* 37:17386–17401.

58. Park, C., L. W. Schultz, and R. T. Raines. 2001. Contribution of the active site histidine residues of ribonuclease A to nucleic acid binding. *Biochemistry.* 40:4949–4956.

59. Finkelstein, A. V., and J. Janin. 1989. The price of lost freedom: entropy of bimolecular complex formation. *Protein Eng.* 3:1–3.

60. Tidor, B., and M. Karplus. 1994. The contribution of vibrational entropy to molecular association—the dimerization of insulin. *J. Mol. Biol.* 238:405–414.

61. Gilson, M. K., J. A. Given, B. L. Bush, and J. A. McCammon. 1997. The statistical-thermodynamical basis for computation of binding affinities: a critical review. *Biophys. J.* 72:1047–1069.

62. Sitkoff, D., K. A. Sharp, and B. Honig. 1994. Accurate calculation of hydration free energies using macroscopic solvent models. *J. Phys. Chem.* 98:1978–1988.

63. Doig, A. J., and M. J. E. Sternberg. 1995. Side-chain conformational entropy in protein folding. *Protein Sci.* 4:2247–2251.

64. Simonson, T., and D. Perahia. 1995. Microscopic dielectric properties of cytochrome-c from molecular dynamics simulations in aqueous solution. *J. Am. Chem. Soc.* 117:7987–8000.

65. Simonson, T. 1998. The dielectric constant of cytochrome-c from simulations in a water droplet including all electrostatic interactions. *J. Am. Chem. Soc.* 120:4875–4876.

66. Pitera, J. W., M. Falta, and W. F. van Gunsteren. 2001. Dielectric properties of proteins from simulations: the effects of solvent, ligands, pH, and temperature. *Biophys. J.* 80:2546–2555.

67. Stern, H. A., and S. E. Feller. 2003. Calculation of the dielectric permittivity profile of a nonuniform system: application to a lipid bilayer simulation. *J. Chem. Phys.* 118:3401–3412.

68. Ballenegger, V., and J. P. Hansen. 2005. Dielectric permittivity profiles of confined polar fluids. *J. Chem. Phys.* 122:114711.

69. Warshel, A., S. T. Russell, and A. K. Churg. 1984. Macroscopic models for studies of electrostatic interactions in proteins: limitations and applicability. *Proc. Natl. Acad. Sci. USA.* 81:4785–4789.

70. Schutz, C. N., and A. Warshel. 2001. What are the dielectric constants of proteins and how to validate electrostatic models. *Proteins Struct. Funct. Bioinf.* 44:400–417.

71. Eberini, I., A. Baptista, E. Gianazza, F. Fraternali, and T. Beringhelli. 2004. Reorganization in apo- and holo-β-lactoglobulin upon protonation of Glu^{89}: molecular dynamics and pK_a calculations. *Proteins Struct. Funct. Bioinf.* 54:744–758.